Front. Energy 2023, 17(2): 228–238
https://doi.org/10.1007/s11708-022-0852-6

RESEARCH ARTICLE

Weishuo SHI, Jinwei HE

Fault tolerant control strategy for modular PWM current source inverter

Abstract In this paper, a fault-tolerant control method for an input-series output-parallel modular grid-tied pulse-width modulation (PWM) current source inverter is proposed to address the most commonly seen single symmetrical gate-commutated thyristor (SGCT) open-circuit fault problems. This method actively offsets the neutral point of the current space vector to ensure a sinusoidal output of the grid current, and it can achieve the upper limit power of the inverter under the condition of a single SGCT open-circuit fault. In addition, an active damping control method based on grid harmonic current feedback is proposed after analyzing the influence of the transformer ferromagnetic resonance caused by the neutral point offset on the power quality of the grid current. It has been demonstrated that the proposed method effectively suppresses the resonance caused by the transformer and the modified modulation, improving the grid current's power quality.

Keywords current source converter (CSC), fault-tolerant control, space vector modulation, active damping, resonance suppression, power quality

1 Introduction

As a large amount of renewable energy, such as wind and solar power, is widely applied in power generation, grid-tied inverter technology in power electronics has developed rapidly [1–3]. PWM current source inverters provide the advantages of simple structure and control, good short-circuit characteristics, and high output waveform quality; therefore, they have received increasing attention in new distributed generation systems, energy storage systems, power flow control [4–6]. With the increase in voltage and power levels, a single inverter cannot meet the requirements of system power capacity; therefore, research has been conducted on the modular current source inverter (CSI) and its control method [7,8].

Compared to a single CSI, a modular CSI has more power switches and thus has more potential for faults. The fault of the switches will not only cause serious distortion of the grid current waveform but also adversely affect the grid's stability. Generally, the fault of switches can be divided into short-circuit fault and open-circuit fault [9]. In fact, open-circuit faults caused by the damage of the power switch itself and the loss of trigger pulses are more commonly observed. Therefore, it is of great theoretical and practical significance to study the open-circuit fault-tolerant control of modular CSI and ensure its upper limit power output under fault conditions.

A large number of open-circuit fault diagnosis and tolerant control methods have been proposed [10–15], but they primarily focus on voltage source converters (VSCs), such as cascaded H-bridges and T-type three-level inverters. In Ref. [10], a cascaded H-bridge converter with redundant modules was proposed, and the faulty module could be bypassed online using a switch. In Ref. [11], the fundamental output voltage of the cascaded H-bridge was controlled by looking up the offline table for the amplitude and phase angle, while the third and fifth harmonics were eliminated using specific harmonic elimination methods. In Ref. [12], the average line voltage deviation on the inverter side was compared with the threshold value during a sampling period to accurately diagnose IGBT (Insulated Gate Bibolar Transistor) open-circuit faults in T-type three-level inverters without adding additional hardware circuits.

Although fault-tolerant control methods for VSCs have been relatively mature, research on current source converters (CSCs) has primarily focused on optimizing modulation methods, power distribution, and common-mode

Received May 5, 2022; accepted Aug. 31, 2022; online Dec. 30, 2022

Weishuo SHI (✉), Jinwei HE (✉)
School of Electrical and Information Engineering, Tianjin University, Tianjin 300072, China
E-mails: shiweishuo@tju.edu.cn (Weishou SHI);
jinwei.he@tju.edu.cn (Jinwei HE)

Special Column: Microgrids and Integrated Energy Systems

voltage suppression [2–8]. There are still few studies on fault-tolerant control of CSC. Guo et al. [13] diagnosed short-circuit faults of a single or double SGCT (Symmetrical Gate-Commutated Thyristor) in CSC by calculating the average values of the feedback output currents and comparing them to the average absolute values of the current reference signals in one power frequency cycle, which can be simply implemented without additional sensors and other auxiliary detection devices. Fard et al. [14] diagnosed the open-circuit fault of current-source inverters in motor drives by the difference between the expected DC current from the PWM signals and the actual DC current and used the redundant branch to replace the faulty one. In Ref. [15], when the five-phase current-source inverter has a broken-line fault, the instantaneous active power fluctuation is reduced by reasonably setting the positive, negative, and pseudo-zero-sequence components of the line current and compensating the current offset of the LC filter, thereby improving the active power transmission capability of the inverter under broken-line faults.

Aiming at the single symmetrical gate-commutated thyristor (SGCT) open-circuit fault of input-series output-parallel modular grid-tied PWM CSI, this paper proposes a fault tolerant control method, which ensures the upper limit power by actively offsetting the neutral point of the reference current vector. Furthermore, based on the analysis of the influence of the transformer ferromagnetic resonance on the grid current, an active damping control method based on the grid harmonic current feedback is proposed to suppress the ferromagnetic resonance and improve the power quality of the grid current.

2 Fault-tolerant modulation of input-series output-parallel CSC

A typical input-series output-parallel modular CSI topology is illustrated in Fig. 1. CSC1 and CSC2 are

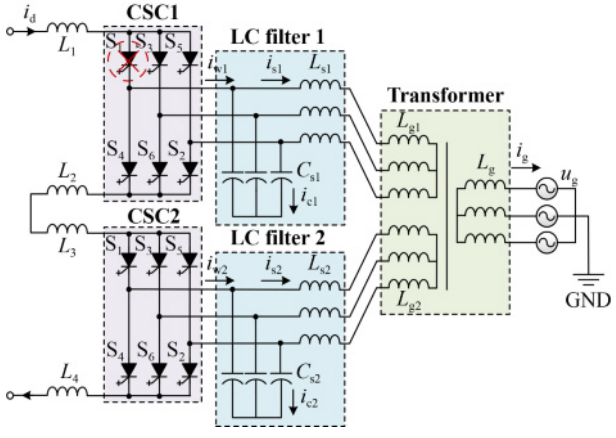

Fig. 1 Configuration of input-series output-parallel modular CSI.

three-phase full-bridge modules composed of SGCT. Two modules are connected in series on the DC side, while on the AC side, they are connected in parallel through their respective LC filter and a Yy-Type three-winding transformer and then connected to the grid. The DC link current is i_d and behaves as a current source. The upper and lower DC rail inductors of CSC1 are L_1 and L_2 respectively, the output PWM current of CSC1 is i_{w1}, and the capacitor and inductor of LC filter 1 are respectively C_{s1} and L_{s1}. The capacitor current is i_{c1}, and the inductor current is i_{s1}. In contrast, the upper and lower DC rail inductors of CSC2 are L_3 and L_4 respectively, the output PWM current is i_{w2}, and the capacitor and inductor of LC filter 2 are respectively C_{s2} and L_{s2}. The capacitor current is i_{c2}, and the inductor current is i_{s2}. The leakage inductors of the transformer windings connected to the two LC filters are L_{g1} and L_{g2} respectively, and the leakage inductor of the windings connected to the grid is L_g. The three-phase grid voltage is u_g and the grid current is i_g. The transformer is mainly used to isolate the DC component of the output PWM current, which is explained in detail later. In addition, it can connect two inverters in parallel on the grid side and isolate the inverter from the grid to effectively reduce the common-mode voltage of the system.

According to the switching constraints of the CSC, only two switches are turned on at any time for each bridge, one in the upper and the other in the lower. Therefore, there are 81 switching states for the above input-series output-parallel CSC, and all the switching states can be divided into 19 PWM current vectors ($I_0 - I_{18}$) according to the level of the total three-phase output PWM current (the sum of the CSC1 and CSC2 output PWM currents, which is $i_{w1}+i_{w2}$). The corresponding three-phase total-output PWM current levels and switching states are listed in Table 1. In the table, the number of arrays represents the number of switches being turned on. For instance, the switching state (16:16) indicates that switches S1 and S6 of CSC1 and switches S1 and S6 of CSC2 are turned on.

Figure 2(a) shows the space vector diagram of the modular CSI under normal operating conditions. The three-phase instantaneous output PWM current is represented by a rotating reference current vector, $\vec{I}_{ref}$, and the grid current can be controlled by adjusting $\vec{I}_{ref}$. All the current vectors in Table 1 can be utilized to synthesize $\vec{I}_{ref}$ based on the ampere-second balance principle, and $\vec{I}_{ref}$ is generally synthesized by three nearby vectors.

When the modular CSI has a single SGCT open-circuit fault, for instance, S1 in CSC1, A-phase output current of CSC1 cannot output the I_d level owing to the S1 open-circuit fault; therefore, some switching states cannot be utilized to synthesize $\vec{I}_{ref}$. All current vectors and switching states that cannot be utilized are marked in red

font in Table 1. It can be seen that I_1, I_2, and I_7 are not available, and $I_8, I_{12}, I_{13}-I_{18}$, and I_0 also lose some switching states, as shown in Table 1.

The current space vector diagram for the S1 open-circuit fault condition is shown in Fig. 2(b). After the loss of I_1, I_2, and I_7, the reference current vector can only operate in the purple area in Fig. 2(b). If the neutral point of the reference current vector is actively offset from point O to point O′ and the reference current vector operates within the circle in Fig. 2(b), the grid current can still be controlled as a sinusoidal output. In addition, the output power can be maximized under an S1 open-circuit fault condition. $\vec{I}_{\text{off}}$ is the active offset vector and $\vec{I}_{\text{ref}'}$ is the current reference vector with the O' point as the center of the circle trace after the active offset. $\vec{I}_{\text{ref}}$ is the current reference vector synthesized during the modulation and still centers at the O point. The three current vectors above satisfy:

$$\vec{I}_{\text{ref}} = \vec{I}_{\text{ref}'} + \vec{I}_{\text{off}}, \tag{1}$$

where the active offset vector $\vec{I}_{\text{off}}$ is:

$$\vec{I}_{\text{off}} = \frac{\sqrt{3}}{4} I_{\text{d}} \mathrm{e}^{-\mathrm{j}\pi}. \tag{2}$$

Therefore, the normal modulation mode can be switched to the fault-tolerant modulation mode by actively offsetting the neutral point and superimposing the offset vector $\vec{I}_{\text{off}}$ on $\vec{I}_{\text{ref}'}$. When $\vec{I}_{\text{ref}'}$ rotates on the circle in Fig. 2(b), the output PWM current of the modular CSI under a single-SGCT open-circuit fault condition is maximized, and the transmission power has an upper limit. At the same time, the modulation factor (m_{a}) is 0.65, which is much larger than that when the faulty module is directly shut down. Notably, the marked operating circle in Fig. 2(b) is the inscribed circle of the purple area, which represents the power transmission limit of the system under the condition of a single SGCT open-circuit fault. If the transmission power continues to increase, the operating circle will exceed the purple area, the output PWM current waveform will be distorted, and the desired power will not be output. Therefore, the fault-tolerant control method proposed in this study effectively improves the power transmission capability of the modular CSI and ensures the upper limit power output under open-fault conditions.

Table 1 Current vectors and their corresponding total output current and switching states

Current vector	Total output PWM current (i_{wa} i_{wb} i_{wc})	Switching state
I_1	(2 –2 0)*i_{d}	16:16
I_2	(2 0 –2) *i_{d}	12:12
I_3	(0 2 –2) *i_{d}	32:32
I_4	(–2 2 0) *i_{d}	34:34
I_5	(–2 0 2) *i_{d}	54:54
I_6	(0 –2 2) *i_{d}	56:56
I_7	(2 –1 –1) *i_{d}	16:12 12:16
I_8	(1 1 –2) *i_{d}	12:32 32:12
I_9	(–1 2 –1) *i_{d}	32:34 34:32
I_{10}	(–2 1 1) *i_{d}	34:54 54:34
I_{11}	(–1 –1 2) *i_{d}	54:56 56:54
I_{12}	(1 –2 1) *i_{d}	56:16 16:56
I_{13}	(1 –1 0) *i_{d}	16:14 14:16 16:36 36:16 56:12 12:56 52:16 16:52
I_{14}	(1 0 –1) *i_{d}	12:14 14:12 12:52 52:12 36:12 12:36 32:16 16:32
I_{15}	(0 1 –1) *i_{d}	32:36 36:32 32:52 52:32 34:12 12:34 32:14 14:32
I_{16}	(–1 1 0) *i_{d}	34:36 36:34 14:34 34:14 54:32 32:54 52:34 34:52
I_{17}	(–1 0 1) *i_{d}	54:14 14:54 54:52 52:54 54:36 36:54 56:34 34:56
I_{18}	(0 –1 1) *i_{d}	56:52 52:56 56:36 36:56 54:16 16:54 56:14 14:56
I_0	(0 0 0) *i_{d}	14:14 36:36 52:52 14:36 14:52 36:52 36:14 52:14 52:36 16:34 12:54 32:56 34:16 54:12 56:32

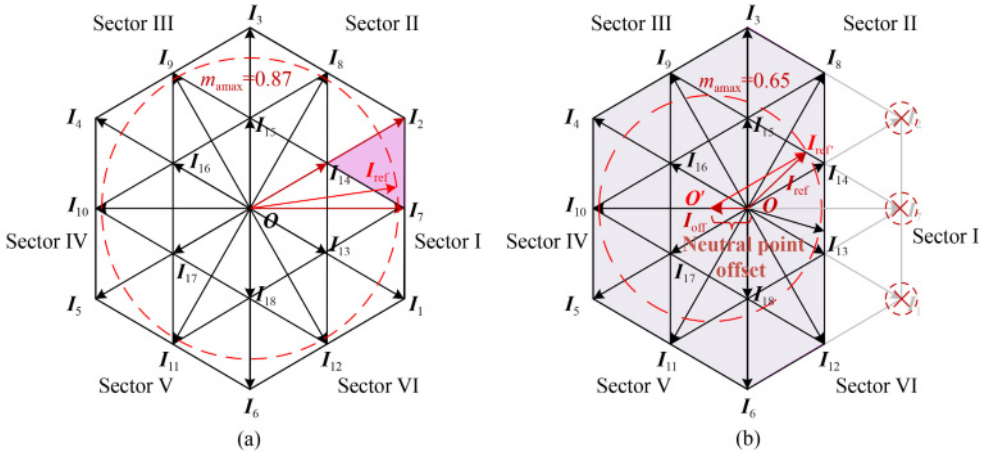

Fig. 2 Current space vector diagram for different modulation modes.
(a) Current space vector diagram for normal operation modulation; (b) current space vector diagram for fault tolerant modulation,

It should be noted that the active offset vector $\vec{I}_{\text{off}}$ introduces a DC component into the three-phase output PWM current. However, its DC component cannot generate an alternating magnetic field in the transformer and, therefore, will not be transformed to the grid side. When other switches in the modular CSI have an open-circuit fault, the proposed fault-tolerant method can also be used; only the active offset vector $\vec{I}_{\text{off}}$ is different. Table 2 lists the expression of $\vec{I}_{\text{off}}$ for all switches in the case of a single SGCT open-circuit fault.

3 Resonance analysis and control strategy

When a large DC current flows through the transformer, the core of the transformer transitions to the saturation region. However, capacitive components in the system are highly prone to ferromagnetic resonance with the nonlinear equivalent inductor of the transformer [16]. Ferromagnetic resonance not only distorts the grid current but also seriously endangers the stability of system operation [17]. Generally, ferromagnetic resonance is caused by fifth, seventh, or other low-order harmonics. Owing to the complex electromagnetic process involved in transformer ferromagnetic resonance, this study utilizes a harmonic current source to simply represent the effect of ferromagnetic resonance on the system instead of describing its process in detail. Considering ferromagnetic resonance, the single-phase equivalent circuit of the system is shown in Fig. 3(a), where R_{s1} and R_{s2} are the internal resistances of the inductor. The Yy-Type three-winding transformer is represented by an ideal transformer and the corresponding winding leakage inductor, whereas a controlled current source represents the ferromagnetic resonance i_h.The output currents of the two CSCs are first filtered by the LC filters and then added in parallel to obtain i_s, which superimposes the harmonic current i_h and flows into the grid; thus, a grid current with large harmonic content is generated. Moreover, the content of the fifth and seventh harmonics in the output current increases under fault conditions owing to the decreaseof m_a, which also affects the power quality of the grid current.

Table 2 Expression of $\vec{I}_{\text{off}}$ for all switches in the case of a single SGCT open-circuit fault

	Faulty switch	$\vec{I}_{\text{off}}$
CSC1	S1	$\sqrt{3}/4I_{\text{d}}\text{e}^{-\text{j}\pi}$
	S2	$\sqrt{3}/4I_{\text{d}}\text{e}^{-\text{j}(2/3\pi)}$
	S3	$\sqrt{3}/4I_{\text{d}}\text{e}^{-\text{j}(1/3\pi)}$
	S4	$\sqrt{3}/4I_{\text{d}}$
	S5	$\sqrt{3}/4I_{\text{d}}\text{e}^{\text{j}(1/3\pi)}$
	S6	$\sqrt{3}/4I_{\text{d}}\text{e}^{\text{j}(2/3\pi)}$
CSC2	S1	$\sqrt{3}/4I_{\text{d}}\text{e}^{-\text{j}\pi}$
	S2	$\sqrt{3}/4I_{\text{d}}\text{e}^{-\text{j}(2/3\pi)}$
	S3	$\sqrt{3}/4I_{\text{d}}\text{e}^{-\text{j}(1/3\pi)}$
	S4	$\sqrt{3}/4rmI_{\text{d}}$
	S5	$\sqrt{3}/4I_{\text{d}}\text{e}^{\text{j}(1/3\pi)}$
	S6	$\sqrt{3}/4I_{\text{d}}\text{e}^{\text{j}(2/3\pi)}$

For further analysis, the equivalent circuit of the system is first simplified. Assuming that the two LC filters have the same parameters and the transformer windings connected to the LC filters also have exactly the same leakage inductor, that is, $C_{s1}=C_{s2}, L_{s1}=L_{s2}, R_{s1}=R_{s2}$, and $L_{g1}=L_{g2}$. Ignoring the transformer's voltage transformation function, the equivalent circuit shown in Fig. 3(a) can be simplified to the equivalent circuit in Fig. 3(b), where

$$\begin{cases} i_{\text{w}} = i_{\text{w1}} + i_{\text{w2}}, \\ L_{\text{s}} = \dfrac{1}{2}(L_{\text{s1}} + L_{\text{g1}}) = \dfrac{1}{2}(L_{\text{s2}} + L_{\text{g2}}), \\ R_{\text{s}} = \dfrac{1}{2}R_{\text{s1}} = \dfrac{1}{2}R_{\text{s2}}, \\ C_{\text{s}} = 2C_{\text{s1}} = 2C_{\text{s2}}. \end{cases} \tag{3}$$

Two CSIs that first pass through their respective LC filters and then connect in parallel are completely equivalent to those first connected in parallel and then passing through a common LC filter.

To suppress LC resonance in CSC, the capacitor voltage or inductor voltage is generally used as the inner-loop feedback, which is equivalent to a virtual resistance connected in parallel to the capacitor or inductor [18]. However, this method cannot be used to suppress the ferromagnetic resonance of transformers. An active

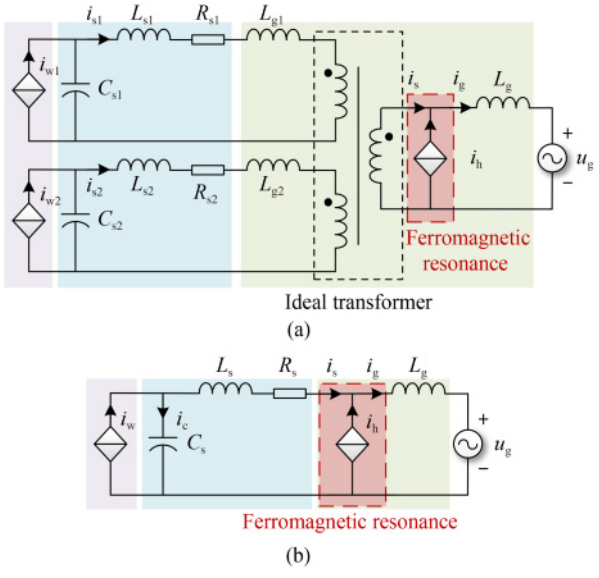

Fig. 3 Single-phase equivalent circuit considering transformer ferromagnetic resonance.

(a) Single-phase equivalent circuit; (b) simplified single-phase equivalent circuit.

damping method based on grid harmonic current feedback is proposed in this paper, and the system control block diagram combined with the proposed fault-tolerant modulation strategy is shown in Fig. 4.

First, the three-phase grid current i_g is transformed from the three-phase stationary frame to the αβ frame to obtain $i_{g\alpha}$ and $i_{g\beta}$. Subsequently, $i_{g\alpha}$ and $i_{g\beta}$ are compared with the reference currents $i^*_{g\alpha}$ and $i^*_{g\beta}$, and the difference is used as the input of the PR controller to control the fundamental current. Feedforward control is implemented from the reference current to the modulation input to improve the system's dynamic response. Therefore, the fundamental current modulation inputs i_{α_ref1} and i_{β_ref1} are produced by

$$i_{\alpha\_ref1} = i^*_{g\alpha} + (i^*_{g\alpha} - i_{g\alpha}) \cdot \left(k_p + \frac{2k_r\omega_r s}{s^2 + 2\omega_r s + \omega_0{}^2} \right), \quad (4)$$

$$i_{\beta\_ref1} = i^*_{g\beta} + (i^*_{g\beta} - i_{g\beta}) \cdot \left(k_p + \frac{2k_r\omega_r s}{s^2 + 2\omega_r s + \omega_0{}^2} \right), \quad (5)$$

where k_p and k_r are the proportional and resonant gains of the PR controller, respectively, ω_r is the bandpass frequency of the resonant controller, ω_0 is the fundamental angular frequency.

Second, the grid current $i_g^{\alpha\beta}$ is filtered by a high-pass filter with a cutoff frequency ω_c:

$$i^{\alpha\beta}_{g\_HPF} = i^{\alpha\beta}_g \cdot \frac{s}{s + \omega_c}. \quad (6)$$

Multiplying $i^{\alpha\beta}_{g\_HPF}$ by the feedback coefficient k, we obtain the damping current $i_k^{\alpha\beta}$, which is also the harmonic current modulation input i_{α_ref2} and i_{β_ref2}.

Then, two modulation inputs are added to obtain the final reference currents i_{α_ref} and i_{β_ref} and transformed from the $\alpha\beta$ frame back to the three-phase stationary frame to produce the reference current $\vec{I}_{ref'}$, which can be utilized for space vector modulation (SVM) according to the modulation mode. When the system is in normal operation, the reference current $\vec{I}_{ref'}$ can be directly utilized for modulation. When the system has a single SGCT open-circuit fault, $\vec{I}_{off}$ is added to the reference current $\vec{I}_{ref'}$. $\vec{I}_{off}$ can be obtained from Table 2 based on the faulty switch.

Finally, the current vector is selected to generate the corresponding gate signal based on the ampere-second balance principle, which controls the turn-on and turn-off of CSI power switches.

Figure 5 shows the transfer function diagram of the system after introducing active damping control. Transformer ferromagnetic resonance is represented by a seventh harmonic current source, and its equivalent transfer function G_{Ih} can be expressed as

$$G_{Ih} = \frac{2k_h\omega_{cut}s}{s^2 + 2\omega_{cut}s + \omega_h^2}, \quad (7)$$

where k_h, ω_h, and ω_{cut} are the harmonic gain, harmonic angular frequency, and bandpass frequency, respectively. The active damping loop gain $G_{AD}(s)$ is expressed as follows:

$$G_{AD}(s) = k \cdot \frac{s}{s + \omega_c} = \frac{ks}{s + \omega_c}. \quad (8)$$

The other transfer functions are expressed according to the equivalent circuit shown in Fig. 3(b) as follows:

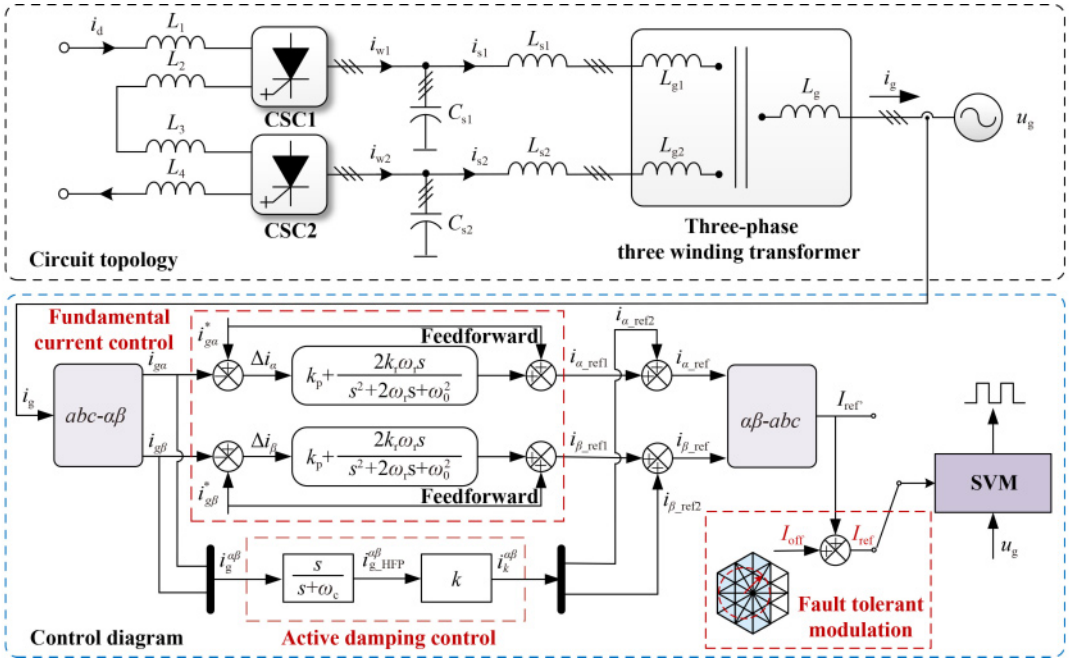

Fig. 4 Fault tolerant and active damping control diagram for input-series output-parallel CSI.

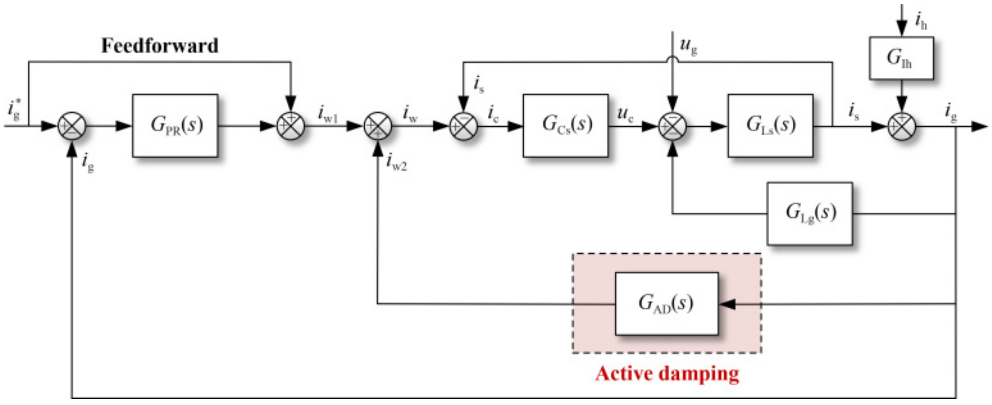

Fig. 5 Transfer function diagram after introducing active damping control.

$$\begin{cases} G_{Cs}(s)=\dfrac{1}{C_s s}, \\ G_{Lg}(s)=L_g s, \\ G_{Ls}(s)=\dfrac{1}{L_s s+R_s}. \end{cases} \tag{9}$$

Therefore, the system transfer function can be expressed as

$$i_g=\frac{G_{Ih}(1+G_{Cs}G_{Ls})}{M}i_h+\frac{G_{Cs}G_{Ls}(1+G_{PR})}{M}i_g^*-\frac{G_{Ls}}{M}u_s, \tag{10}$$

where

$$M=1+(G_{Lg}+G_{Cs})G_{Ls}+G_{Cs}G_{Ls}(G_{PR}-G_{AD}). \tag{11}$$

To analyze the suppression effect of the proposed active damping control method on the ferromagnetic resonance and LC filter resonance, the closed-loop Bode diagram of the system with different feedback coefficients k is plotted, as shown in Figs. 6–8. Figure 6 shows the closed-loop Bode diagram of the transfer function i_g/i_h when k increases from 0 to 0.2. When active damping control is not introduced, a large resonance peak appears at approximately 350 Hz, which is close to the ferromagnetic resonance frequency of the transformer. As the feedback coefficient k increased, the ferromagnetic resonance peak gradually decreased, and the ferromagnetic resonance was effectively suppressed. When k is sufficiently large, the ferromagnetic resonance peak decreases significantly, and the active damping effect is highly effective.

Closed-loop Bode diagrams of the transfer functions i_g/i_g^* and i_g/u_g are shown in Fig. 7 and Fig. 8, respectively. When k = 0, a resonance peak appears at approximately 350 Hz. With an increase in k, the resonant peak of the system gradually decreased, the resonant peak frequency decreased slightly, and the system had a larger bandpass frequency. However, when k is sufficiently large, it causes a large phase shift between the fundamental and resonant frequencies.

Therefore, the active damping control method proposed in this study has a positive damping effect on the ferromagnetic resonance of the transformer. 0.1 is chosen as the feedback coefficient k in this study to have a significant damping effect.

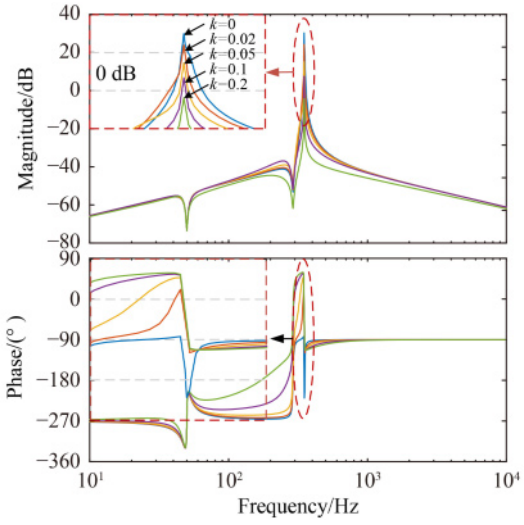

Fig. 6 Closed-loop bode diagram of transfer function i_g/i_h with different k.

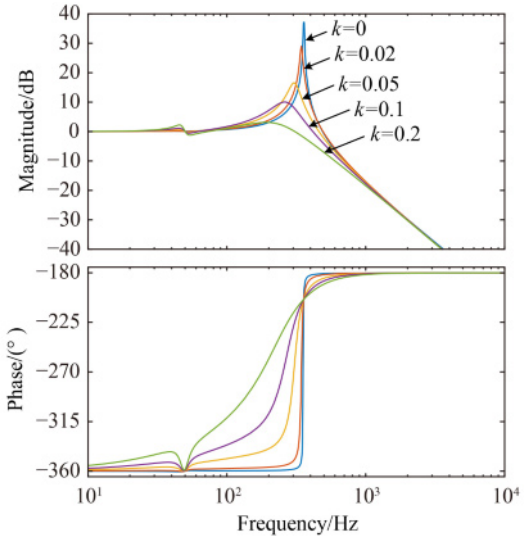

Fig. 7 Closed-loop bode diagram i_g/i_g^* with different k.

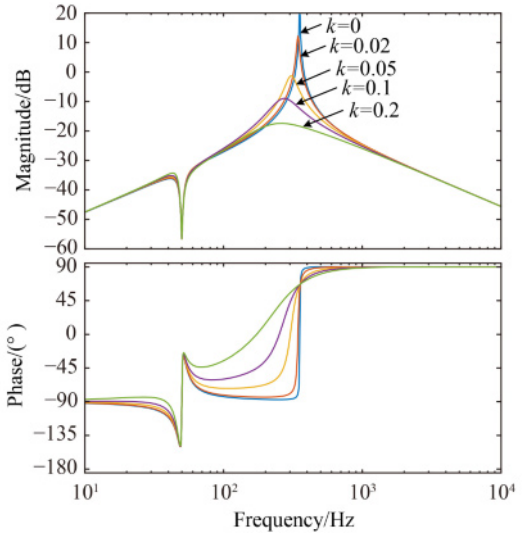

Fig. 8 Closed-loop bode diagram i_g/u_g with different k.

4 Simulation results

A simulation model was built for simulation verification in MATLAB/Simulink to verify the effectiveness of the proposed fault-tolerant modulation and active damping method. The key simulation parameters are listed in Table 3. The modular CSC transmits a constant active power of 48 kW and operates with a unit power factor under healthy operating conditions. In the case of a single SGCT open-circuit fault, the transmitted active power must be reduced; however, the unit power factor is still maintained. The ferromagnetic resonance was simulated using a harmonic-controlled current source.

The simulation is divided into four stages to verify the proposed fault-tolerant modulation and active damping methods. A brief description of these four stages is given in Table 4, and the full-stage simulation results are shown in Fig. 9.

Stage 1: 0.16–0.2 s, the system operates healthy without any fault. The grid current is approximately 70 A, of great quality, and in the same phase angle as the grid voltage, and the total harmonic distortion (THD) is only 2.08%. The total three-phase output current was a symmetrical five-level PWM current.

Stage 2: 0.2–0.26 s, the system operates under a single SGCT open-circuit fault condition, but fault-tolerant control is not enabled. The grid current of the faulty phase (phase *A*) is seriously distorted with a THD of 23.08%, and the upper peak is cut off, whereas the grid currents of the non-faulty phases (phases *B* and *C*) also have a certain degree of distortion. The total output current of the faulty phase (phase *A*) changes into four asymmetric levels, whereas the total output current of the non-faulty phases (phases *B* and *C*) has more levels. It should be noted that when a single SGCT open-circuit fault occurs without any fault-tolerant control, the switching constraints of the CSC will not be satisfied; therefore, it is not allowed to operate in this case in practice.

Table 3 Key parameters of the simulated system

Circuit parameters	Values
Line grid voltage	380 V/50 Hz
DC link current	50 A
Filter inductor (L_{s1}, L_{s2})	3.4 mH
Filter capacitor (C_{s1}, C_{s2})	50 μF
Leakage inductor on inverter side (L_{g1}, L_{g2})	0.4 mH
Leakage inductor on grid side (L_g)	0.4 mH
Transformer ratio	1:1
Control parameters	**Values**
Switching frequency	4.5 kHz
Proportional gain k_p	k_p =0.5
Resonance gain k_r	k_r =50
Feedback coefficient k	k= 0.1

Table 4 Description of different stages of the CSC

System stage	Faulty	Fault-tolerant modulation	Active damping control
Stage 1	No	No	No
Stage 2	Yes	No	No
Stage 3	Yes	Yes	No
Stage 4	Yes	Yes	Yes

Stage 3: 0.26–0.32 s, The system switches to fault-tolerant modulation without an active damping control. The introduction of an active offset vector restored the grid current of the faulty phase (phase *A*) to a sinusoidal waveform. However, the ferromagnetic resonance of the transformer and the decrease in m_a cause an increase in the harmonic content of the grid current, and the THD of the faulty phase grid current reaches 28.86%. In addition, the active offset vector makes all three phases of the total output current asymmetric.

Stage 4: 0.32–0.38 s, Active damping control is introduced. The resonance was quickly damped, and the grid current entered a new steady state after approximately 30 ms. At this time, the THD of the A-phase grid current decreases to 3.82%. The grid current was only 58 A, owing to the reduced power after the fault-tolerant control. At the same time, the decrease in m_a results in more fifth and seventh harmonics in the output current [19]; therefore, the quality of the grid current waveform decreases slightly compared to that under normal operation.

To further verify the effectiveness of the proposed method, we carried out hardware-in-the-loop simulations, and the detailed circuit and control parameters in the hardware-in-the-loop simulation are listed in Table 5.

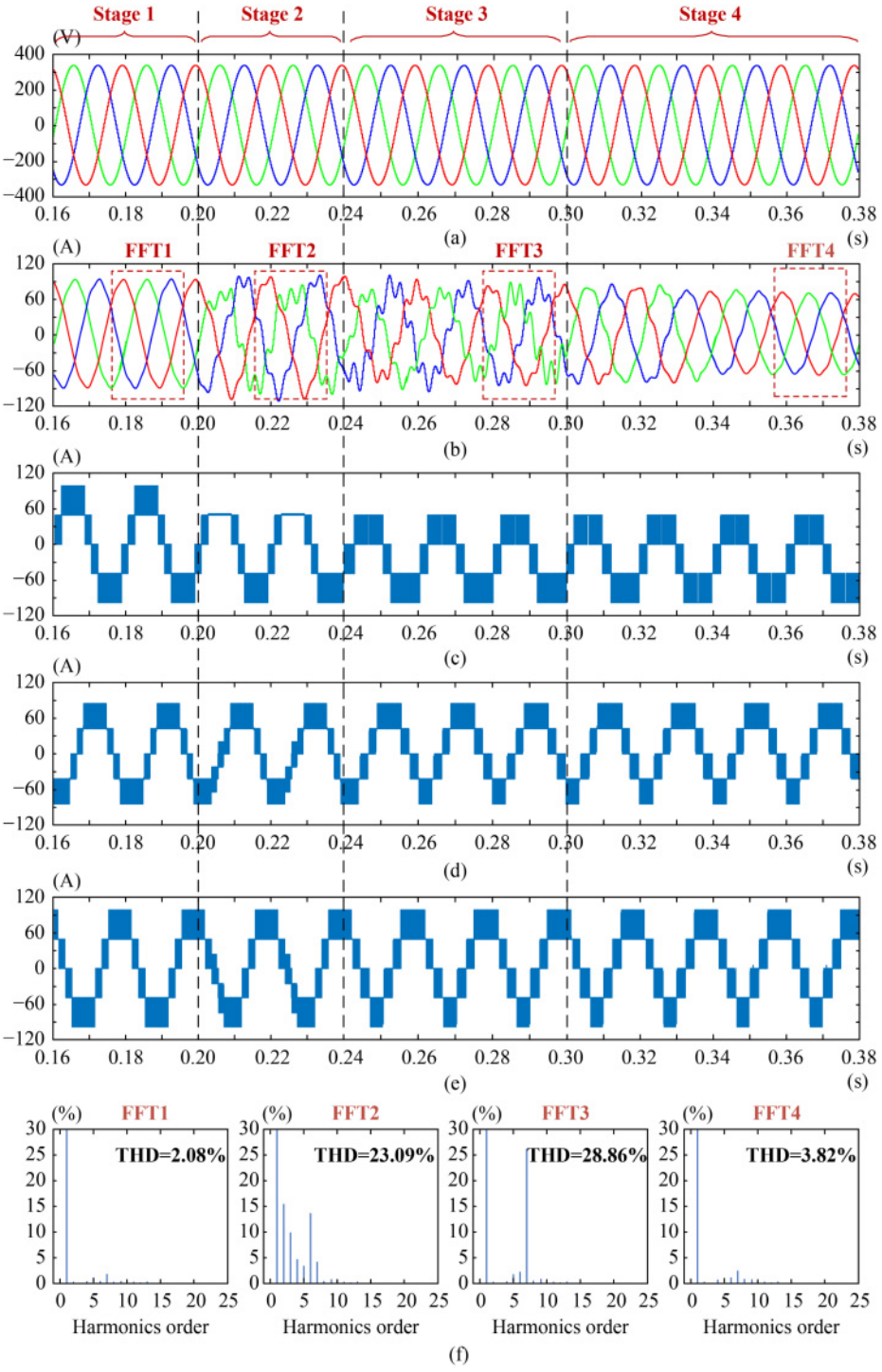

Fig. 9 Simulated results for the system from healthy operation to fault-tolerant operation.

(a) Three-phase grid voltage; (b) three-phase grid current; (c) total output PWM current of phase *A* (faulty phase); (d) total output PWM current of phase *B* (non-faulty phase); (e) total output PWM current of phase *C* (non-faulty phase); (f) FFT results of *A*-phase grid current.

The steady state of performance using the proposed method in the case of both healthy operations without any fault and fault operation with a single IGCT open circuit is shown in Fig. 10. It can be observed that the grid current has high quality with a low THD of 2.54%, and the three-phase PWM output current is a symmetrical five-level waveform in the case of a healthy operation. In the case of faulty operation with a single IGCT open-circuit, the amplitude of the grid current decreased from 29 to 23 A due to the limited power transmission capacity of the CSC. Simultaneously, the THD of the grid current decreased slightly to 4.28%. It is evident that although

the output current has only an asymmetrical four-level, the proposed method could still realize the sinusoidal output of the grid current and ensure waveform quality under the single IGCT fault condition.

The dynamic response of CSC during the control method switches is shown in Fig. 11. The proposed method has been verified via a total of three stages, in which at stage 1, the CSC operates without any faults; stage 2 switches to the proposed fault-tolerant modulation method without adding active damping control, whereas, at stage 3, the fault-tolerant modulation method is maintained and active damping control is added.

In stage 1, the grid current is sinusoidal because no faults occur. In stage 2, CSC switches to fault-tolerant modulation without active damping control. Although the neutral point of the current space vector is actively offset to maintain a sinusoidal output, the ferromagnetic resonance of the transformer causes severe distortion of the three-phase grid current with a THD of 67.2%. This is because the effect of the transformer ferromagnetic resonance was intentionally increased in the hardware-in-the-loop simulation. In stage 3, with the introduction of active damping control, the ferromagnetic resonance of the transformer is gradually suppressed, and the transient process is only 40 ms. Due to the power transmission capacity limitation and the modulation factor m_a reduction, both the amplitude and quality of the grid current decrease.

The dynamic performance of the proposed method in the case of grid voltage dips is shown in Fig. 12. When the grid voltage drops by 0.2 pu, the grid current is slightly distorted in the transient process, but the system enters a new steady state after only 25 ms. It should be noted that when the CSC operates using the proposed fault-tolerant control method under the single IGCT open-circuit fault condition, the modulation factor of the CSC is already close to the maximum value; therefore, the grid current will not increase, and the transmission power will be further reduced.

Table 5 Key parameters in hardware-in-the-loop simulation

Circuit parameters	Values
Line grid voltage	100 V/50 Hz
DC link current	25 A
Filter inductor (L_{s1}, L_{s2})	2 mH
Filter capacitor (C_{s1}, C_{s2})	50 μF
Leakage inductor on inverter side (L_{g1}, L_{g2})	40 μH
Leakage inductor on grid side (L_g)	4 μH
Transformer ratio	1:1
Control parameters	**Values**
Switching frequency	5 kHz
Proportional gain k_p	k_p =0.1
Resonance gain k_r	k_r =20
Feedback coefficient k	k = 0.1

5 Conclusions

This study proposes a fault-tolerant control method for input-series output-parallel modular CSCs with a single SGCT open-circuit fault, which achieves a sinusoidal output of the grid current under fault conditions by actively offsetting the output current space vector neutral point. In addition, to suppress the transformer ferromagnetic resonance, an active damping control method with grid harmonic current feedback was proposed to ensure the quality of the grid current.

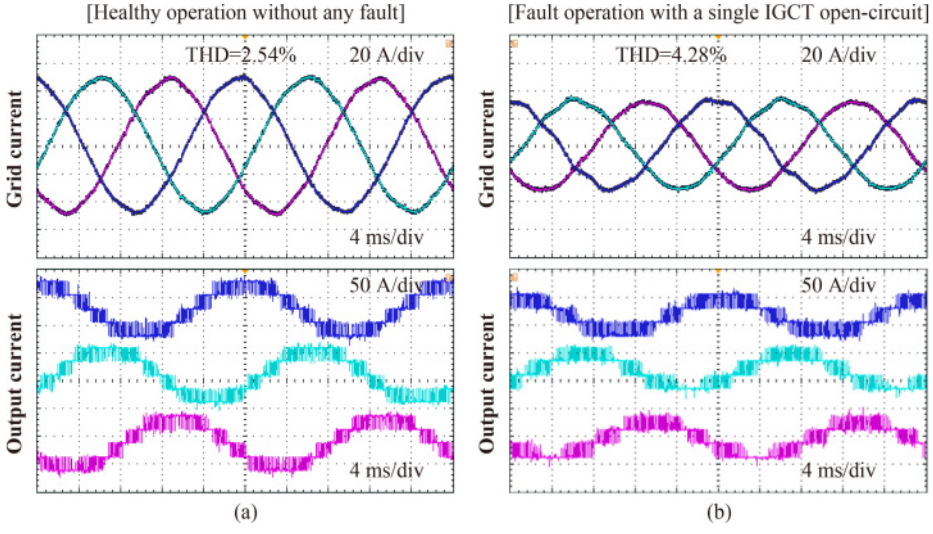

Fig. 10 CSC steady state performance using the proposed method under the case of (a) healthy operation without any fault and (b) fault operation with a single IGCT open-circuit.

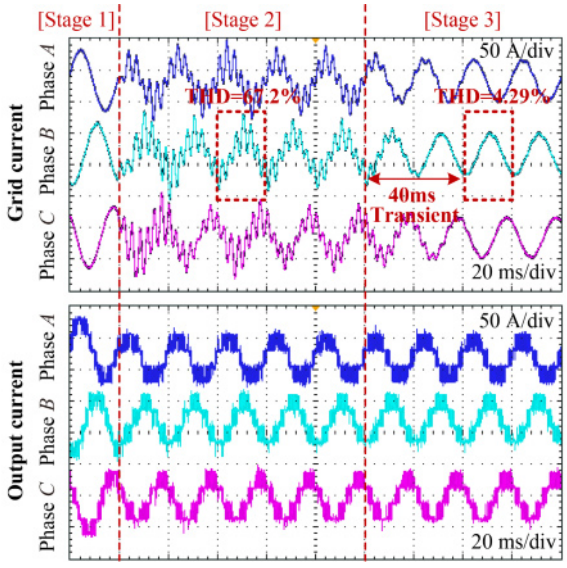

Fig. 11 CSC dynamic response during control method switches.

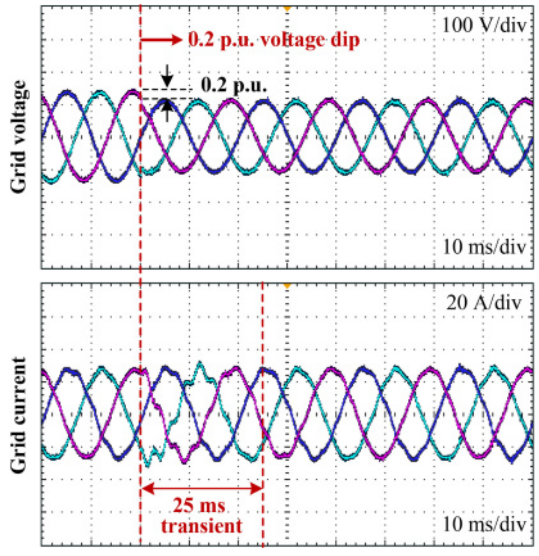

Fig. 12 CSC dynamic performance using the proposed method under the case of grid voltage dips.

However, it should be noted that the proposed method can only be applied to two CSC modules with input-series and output-parallel topologies, and the system's scalability is limited to a certain extent. Therefore, it is necessary to further research the fault-tolerant control of multiple CSC modules with input-series, output-parallel, and other topologies and to propose a general fault-tolerant control method applied to various modular CSC topologies.

Notations

SGCT	Symmetrical gate-commutated thyristor
CSC	Current source converter
CSI	Current source inverter
VSC	Voltage source converter
CSC1, CSC2	Signle current source converter module
i_d	DC link current
L_1, L_2, L_3, and L_4	Upper and lower DC rail inductors of CSC1 and CSC2
i_{w1}, i_{w2}	PWM output current of CSC1 and CSC2
C_{s1}, L_{s1}, C_{s2}, L_{s2}	The capacitor and inductor of the LC filter 1 and LC filter 2
i_{c1}, i_{c2}	Capacitor current of the LC filter 1 and LC filter 2
i_{s1}, i_{s2}	Inductor current of the LC filter 1 and LC filter 2
L_{g1}, L_{g2}, L_g	The leakage inductors of the transformer windings
u_g, i_g	Three-phase grid voltage and grid current
R_{s1}, R_{s2}	The internal resistance of the inductor L_{s1} and L_{s2}
S1–S6	SGCT of CSC1 or CSC2
I_0–I_{18}	PWM current vectors
I_{off}	Active offset vector
I_{ref}'	The current reference vector with the O' point as the center of the circle trace after the active offset
I_{ref}	The current reference vector actually synthesized during the modulation
m_a	Modulation factor
i_h	Harmonic currents generated by transformer ferromagnetic resonance
i_w, L_s, C_s, R_s	The equivalent parameters in the equivalent circuit
$i_{g\alpha}$, $i_{g\beta}$	α-axis, and β-axis components of i_g in the $\alpha\beta$ reference frame
$i^*_{g\alpha}$, $i^*_{g\beta}$	α-axis, and β-axis components of reference grid current.
i_{α_ref1}, i_{β_ref1}	α-axis, and β-axis components of the fundamental current modulation input
i_{α_ref2}, i_{β_ref2}	α-axis, and β-axis components of the harmonic current modulation inputs
k_p, k_r, ω_r, and ω_0	The proportional gain, resonant gain, bandpass frequency, and fundamental angular frequency, respectively, of the PR controller
ω_c	Cutoff frequency of the high-pass filter
k	Feedback coefficient
k_h, ω_h, ω_{cut}	Harmonic gain, harmonic angular frequency, and bandpass frequency of the equivalent transfer function of the transformer ferromagnetic resonance
$i^{\alpha\beta}_{g\_HPF}$	Grid current after a high-pass filter
$i^{\alpha\beta}_k$	Damping current

References

1. Guo X, Yang Y, Zhu T. ESI: a novel three-phase inverter with leakage current attenuation for transformerless PV systems. IEEE Transactions on Industrial Electronics, 2018, 65(4): 2967–2974
2. Sahan B, Araújo S V, Nöding C, et al. Comparative evaluation of

three-phase current source inverters for grid interfacing of distributed and renewable energy systems. IEEE Transactions on Power Electronics, 2011, 26(8): 2304–2318

3. Kumar G R, Bandaru R K. Single phase PV-fed current source inverter with sinusoidal grid current injection control. In: 2019 International Conference on Electrical, Electronics and Computer Engineering (UPCON), Aligarh, India
4. Wei Q, Wu B, Xu D, et al. An optimized strategy for PWM current source converter based wind conversion systems with reduced cost and improved efficiency. IEEE Transactions on Power Electronics, 2018, 33(2): 1202–1210
5. Wu B, Pontt J, Rodriguez J, et al. Current-source converter and cycloconverter topologies for industrial medium-voltage drives. IEEE Transactions on Industrial Electronics, 2008, 55(7): 2786–2797
6. Wei Q, Wu B, Xu D, et al. A new configuration using PWM current source converters in low-voltage turbine-based wind energy conversion systems. IEEE Journal of Emerging and Selected Topics in Power Electronics, 2018, 6(2): 919–929
7. Xu D, Zargari N R, Wu B, et al. A medium voltage AC drive with parallel current source inverters for high power applications. In: 2005 IEEE 36th Power Electronics Specialists Conference, Dresden, Germany
8. He J, Li Q, Zhang C, et al. Quasi-selective harmonic elimination (Q-SHE) modulation-based DC current balancing method for parallel current source converters. IEEE Transactions on Power Electronics, 2019, 34(8): 7422–7436
9. Lu B, Sharma S K. A literature review of IGBT fault diagnostic and protection methods for power inverters. IEEE Transactions on Industry Applications, 2009, 45(5): 1770–1777
10. Neyshabouri Y, Iman-Eini H. A new fault-tolerant strategy for a cascaded H-bridge based STATCOM. IEEE Transactions on Industrial Electronics, 2018, 65(8): 6436–6445
11. Song W, Huang A Q. Fault-tolerant design and control strategy for cascaded H-bridge multilevel converter-based STATCOM. IEEE Transactions on Industrial Electronics, 2010, 57(8): 2700–2708
12. Chen Y, Du L, He J. Online diagnosis and ride-through operation for cascaded H-bridge converter based STATCOM with a single open-circuit IGBT. IEEE Transactions on Industrial Electronics, 2022, 69(8): 7549–7559
13. Guo X, Sui S, Wang B, et al. A current-based approach for short-circuit fault diagnosis in closed-loop current source inverter. IEEE Transactions on Industrial Electronics, 2020, 67(9): 7941–7950
14. Fard M T, He J, Wang Z. Fault diagnosis and fault-tolerant operation of current source inverter for safety-critical applications. In: 2020 IEEE Transportation Electrification Conference & Expo, Chicago, IL, USA
15. He J, Lyu Y, Li Q, et al. A fault-tolerant operation approach for grid-tied five-phase current-source converters with one-phase supplying wire broken. IEEE Transactions on Power Electronics, 2019, 34(7): 6200–6218
16. Gerber I P, Mwaniki F M, Vermeulen H J. Parameter estimation of a Ferro-resonance damping circuit using pseudo-random impulse sequence perturbations. In: 2021 56th International Universities Power Engineering Conference (UPEC), Middlesbrough, UK
17. Abdelazim Mellik T, Painter F D, Shipp D D, et al. Proactive study and novel mitigation of MV power system damage due to sub-power-frequency Ferro-resonance for a gas plant. IEEE Transactions on Industry Applications, 2018, 54(4): 3991–4000
18. Li Y. Control and resonance damping of voltage-source and current-source converters with LC filters. IEEE Transactions on Industrial Electronics, 2009, 56(5): 1511–1521
19. Wu B. High-Power Converters and AC Drives. New York: Wiley-IEEE Press, 2006